Integrative Biology

PAPER

A vascular injury model using focal heat-induced activation of endothelial cells†

J. L. Sylman,[a] D. T. Artzer,[a] K. Rana[a] and K. B. Neeves*[ab]

Cite this: *Integr. Biol.*, 2015, 7, 801

Received 20th April 2015,
Accepted 7th June 2015

DOI: 10.1039/c5ib00108k

www.rsc.org/ibiology

Endothelial cells (EC) both inhibit and promote platelet function depending on their activation state. Quiescent EC inhibit platelet activation by constitutive secretion of platelet inhibitors. Activated EC promote platelet adhesion by secretion of von Willebrand factor (vWF). EC also secrete an extracellular matrix that support platelet adhesion when exposed following vascular injury. Previous studies of EC–platelet interactions under flow activate entire monolayers of cells by chemical activation. In this study, EC cultured in microfluidic channels were focally activated by heat from an underlying microelectrode. Based on finite element modeling, microelectrodes induced peak temperature increases of 10–40 °C above 37 °C after applying 5–9 V for 30 s resulting in three zones: (1) a quiescent zone corresponded to peak temperatures of less than 15 °C characterized by no EC activation or platelet accumulation. (2) An activation zone corresponding to an increase of 16–22 °C yielded EC that were viable, secreted elevated levels of vWF, and were P-selectin positive. Platelets accumulated in the retracted spaces between EC in the activation zone at a wall shear rate of 150 and 1500 s^{-1}. Experiments with blocking antibodies show that platelets adhere *via* GPIbα–vWF and $\alpha_6\beta_1$–laminin interactions. (3) A kill zone corresponded to peak temperatures of greater than 23 °C where EC were not viable and did not support platelet adhesion. These data define heating conditions for the activation of EC, causing the secretion of vWF and the exposure of a subendothelial matrix that support platelet adhesion and aggregation. This model provides for spatially defined zones of EC activation that could be a useful tool for measuring the relative roles of anti- and pro-thrombotic roles of EC at the site of vascular injury.

Insight, innovation, integration

Endothelial cells (EC) have both pro- and antithrombotic functions that regulate thrombus formation. Among these is the secretion of platelet inhibitors and, upon injury, the expression of adhesive platelet ligands. Most *in vitro* models consider these contrasting functions independently. The *technological innovation* in this study is a microfluidic model of vascular injury that allows for a spatially defined zone of prothrombotic EC surrounded by antithrombotic EC. This was accomplished by the *integration* of a surface microelectrode as a heat source to spatially and temporally activate cells in endothelialized microfluidic channels. The *biological insight* is that heat activated EC support platelet accumulation by secreting von Willebrand factor and receding from each other to reveal a laminin-rich extracellular matrix.

Introduction

Endothelial cells (EC) play a dual role in regulating platelet function. They constitutively secrete the platelet inhibitors nitric oxide (NO), prostacyclin and ADPases in a shear stress dependent manner to ensure that platelets do not spontaneously aggregate in the vasculature.[1] When activated by oxidative, mechanical, or inflammatory stresses EC promote platelet recruitment to the vessel wall by expression of E-selectin and the release of Weibel–Palade bodies. Weibel–Palade bodies contain von Willebrand factor (vWF) and P-selectin which support platelet rolling and accumulation.[2] Activated EC also retract from each other revealing an extracellular matrix consisting of collagen, laminin and fibronectin, among other proteins, that support platelet adhesion and activation.[3,4] The spatial and temporal expression of these pro- and antithrombotic pathways likely determines, in part, the size and growth of a thrombus. Yet, there are no *in vitro* models of platelet function that incorporate a spatially controlled region of EC expressing a prothrombotic phenotype surrounded by EC

[a] *Department of Chemical and Biological Engineering, Colorado School of Mines, 1500 Illinois Street, Golden, CO 80401, USA. E-mail: kneeves@mines.edu; Fax: +01 303 273 3730; Tel: +01 303 273 3191*

[b] *Department of Pediatrics, University of Colorado Denver, Aurora, CO, USA*

† Electronic supplementary information (ESI) available. See DOI: 10.1039/c5ib00108k

region expressing an antithrombotic phenotype. The objective of this study was to develop such a model.

In vitro flow assays for measuring platelet function generally fall into two categories; adhesion to subendothelial matrix proteins and rolling/adhesion to activated EC. In the former, purified proteins are adsorbed to a substrate, typically a glass slide or capillary tube, and blood is perfused at user-defined wall shear rate.[5–9] Collagen, fibrinogen and vWF are the most common proteins used for measuring platelet function and tissue factor can be incorporated to study coagulation as well.[10] Combinations of these and other proteins give a range of platelet adhesion and aggregation responses.[11] Flow assays that include monolayers of cultured EC typically involve stimulation by chemical, mechanical and laser methods.[12–14] For example, exposure to inflammatory agents such as TNF-α and interleukin-1 leads to P-selectin exposure on EC, among other prothrombotic molecules, and the recruitment of platelets.[11,15] Stimulation of endothelialized microfluidic channels with TNF-α and shiga toxin mimics the pathology of microvascular diseases such acute inflammation and hemolytic uremic syndrome.[16] PMA stimulated EC in microvascular networks embedded in collagen gels show the importance of channel geometry on platelet–vWF interactions.[17]

The focal nature of a vascular injury is an important feature in the regulation of thrombus formation. A threshold injury size is needed to support platelet adhesion,[18] initiate coagulation[19,20] and fibrin deposition.[21,22] Moreover, ECs within and adjacent to an injury likely play different roles. Activated ECs within or very close to an injury support thrombus formation *via* secretion and expression of adhesive ligands, while those up and downstream limit platelet accumulation to the injury region. No *in vitro* model that we are aware of captures these different roles of ECs in a focal injury model.

In this study, we describe a vascular injury model where EC cultured within microfluidic channels are focally activated by heat using microelectrodes beneath the channels. This approach allows spatial and temporal control of an EC activation zone that supports platelet adhesion and accumulation surrounded by quiescent EC.

Material and methods

Materials

Human umbilical endothelial cells (HUVEC), F-12K medium, trypsin-EDTA, and penicillin streptomycin (10 000 IU mL^{-1} penicillin, 10 000 μg mL^{-1} streptomycin) solution were from American Type Culture Collection (ATCC, Manassas, VA). PE/Cy5 (480 nm/670 nm) anti-human CD41, annexin V and PE anti-human CD62P antibody were from BioLegend (San Diego, CA). Anti-integrin α_6 antibody (GoH3), anti-human VE Cadherin antibody produced in rabbit, anti-human fibronectin antibody produced in rabbit, anti-human collagen I antibody produced in mouse, anti-human collagen IV antibody produced in mouse, goat anti-mouse IgG H&L (Alexa Fluor® 488) and goat anti-rabbit IgG H&L (DyLight® 594) were obtained from Abcam (Cambridge, MA). Abciximab (ReoPro, Eli Lilly, Indianapolis, IN, USA) was from the University of Colorado Hospital pharmacy. FPR-chloromethylketone (PPACK) (75 μM) collection tubes were from Hematologic Technologies Inc. (Essex Junction, VT). Endothelial cell growth supplement (ECGS), Pluronics F-127, fluorescein isothiocyanate (FITC)-phalloidin, fluorescein diacetate, ethidium bromide, anti-laminin antibody produced in rabbit, laminin from human placenta, bovine fibronectin, standard gold etchant, ammonium hydroxide standard chromium etchant, dimethyl sulfoxide, Triton™ X-100, and dextran from Leuconostoc mesenteroides (M_W 150 000) were from Sigma Aldrich (St. Louis, MO). Gold shot (<4 mm pieces) and chromium shot (0.8 mm–6 mm pieces) were from Kurt J. Lesker Company (Clairton, PA). (Tridecafluoro-1,1,2,2-tetrahydrooctyl)trichlorosilane was purchased from Gelest (Morrisville, PA). Phosphate buffered saline (PBS; 137 mM NaCl, 2.7 mM KCl, 10 mM $Na_2HPO_4{\cdot}2H_2O$, 2 mM KH_2PO_4, pH 7.4), HEPES buffered saline (HBS; 20 mM HEPES, 150 mM NaCl, pH 7.4) and isotonic glucose buffer (5% dextrose, pH 2.7) were made in-house. 4′,6-Diamidino-2-phenylindole, dihydrochloride (DAPI) was obtained from Life Technologies (Carlsbad, CA). Polydimethylsiloxane (PDMS) was from Sylgard 184 (Dow Corning, Midland, MI). Complete cell culture media (includes 100 IU mL^{-1} penicillin, 100 μg mL^{-1} streptomycin, 0.1 mg mL^{-1} heparin, 0.03 mg mL^{-1} ECGS, and 10% fetal bovine serum) and serum free media were made in-house.

Fabrication of microelectrodes

Glass slides were stripped of organic and ionic contaminants by RCA-1 (deionized $H_2O/NH_4OH/H_2O_2$, 5 : 1 : 1) and RCA-2 (deionized $H_2O/HCl/H_2O_2$, 5 : 1 : 1), each for 10 min at 75–80 °C. Chromium (Cr) and gold (Au) were deposited on the glass substrates by thermal evaporation to thicknesses of 10 nm and 75 nm, respectively. Shipley 1813 was spin coated onto the Cr/Au film and patterned by photolithography. The exposed metal was etched with gold etchant (1 : 4 dilution in dH_2O) and a chromium etchant (1 : 6 dilution in dH_2O). Electrodes were insulated with diluted 35 wt% KMPR at 3000 rpm for 45 s (diluted KMPR 1050 with cyclopentanone). KMPR was removed from the contact pads by photolithography and silver epoxy was spread on the contact pads of the electrodes as an adhesive for wiring to the power source (ESI,† Fig. S1).

Thermal infrared camera measurement

A 40 μm slab of PDMS was placed on the surface of insulated microelectrode. An infrared thermal imaging camera (FLIR Exx series, Wilsonville, OR) recorded the surface temperature as a function of voltage and time.

Endothelial cell seeding and culture in microfluidic channels

PDMS microfluidic channels were fabricated using standard methods with KMPR patterned on a silicon wafer as a master.[23] The device consisted of four channels with a width of 1000 μm and height of 100 μm and was bonded to a 40 μm PDMS film (ESI,† Fig. S1). The PDMS film was prepared by spinning 10 : 1 (base : catalyst) PDMS at 1500 rpm on glass slides treated with (tridecafluoro-1,1,2,2-tetrahydrooctyl)trichlorosilane for 3 h under vacuum. The devices were treated with oxygen plasma and then

bonded to the PDMS film, which formed the bottom wall of the channel. Channels were sterilized with 70% ethanol for 10 min, flushed with serum free F-12K and then stored in an incubator for 12–18 h at 37 °C and a relative humidity of 95%. The long incubation was required to ensure that all absorbed ethanol was removed from the PDMS prior to introduction of the cells. Fibronectin (50 μg mL^{-1}) in serum free media was incubated in the channels for 2–4 hours. The channels were rinsed with complete F-12K and seeded with HUVEC at a concentration of 300 000–500 000 cells per mL in 6.25% dextran modified buffer to increase the viscosity to 3.5 cP at 150 s^{-1} as measured by a DHR-3 rheometer (TA Instruments, New Castle, DE). Dextran was added to decrease cell settling and enhance seeding density, staying below the concentration of dextran in which EC viability and attachment is affected.[16,24] Fresh complete F-12K was replaced over the cells on a daily basis. Confluence and tight junctions were achieved within two days and cells were used for experiments within 2–3 days of seeding (ESI,† Fig. S2).

Blood collection and treatment

All blood collection was performed in accordance with the Declaration of Helsinki and under the University of Colorado, Boulder Institutional Review Board approval. Human whole blood was obtained from donors through venipuncture. Donors had not consumed alcohol for 48 h, nor taken any prescription or over-the-counter drugs during the 10 days prior to donation. Five milliliters of whole blood were collected into vacutainers containing the PPACK (75 mM). Samples were incubated with anti-human CD41 at 1 : 25 dilution for 20 min. In some experiments, whole blood was incubated with 100 μg mL^{-1} abciximab (GPIIbIIIa antagonist), anti-CD42b (function blocking antibody, 1 : 50), and/or anti-integrin α_6 (function blocking antibody, 1 : 20) for 20 min at 25 °C.

Measurement of EC recession, activation, and viability

EC were heated for 30 s by applying a potential across the electrode (5–9 V) while complete media was perfused at a wall shear rate of 150 s^{-1}. Complete media was perfused for 2 min after heating and then the cells were fixed with 2% glutaraldehyde. The cells were then rinsed with PBS, permeabilized with 0.2% Triton™ X-100 for 10 min, rinsed with PBS, and incubated with one of the following for 1 h; FITC-phalloidin (0.1 μg mL^{-1}) and DAPI (1 : 1000), anti-vWF (1 : 100), anti-human CD62P antibody (1 : 20) or annexin V (1 : 50). Dead cells were labeled with ethidium bromide (0.2 μg mL^{-1}) prior to fixing. To label tight junctions between the cells, cells were fixed with 2% paraformaldehyde and blocked with 5% BSA for 1 h at 20 °C. The cells were then incubated with a primary anti-VE Cadherin (1 : 200, 0.01% Triton™ X-100 and 1% BSA in PBS) for 90 min at room temperature and labeled with a goat anti-rabbit IgG H&L antibody (40 μg mL^{-1}, 1% BSA in PBS) for 60 min. Cells were imaged with a 60× objective (NA = 0.95) on a confocal microscope (Olympus Fluoview FV10i). EC recession was calculated in ImageJ by thresholding the fluorescent cells and quantifying the area fractions. For ethidium bromide and P-selectin measurements, the number of cells that were P-selectin or ethidium bromide positive was divided by the total number of cells indicated by DAPI. For experiments in which the number of vWF strands were counted, the EC were labeled with anti-vWF 10 min prior to heating and dextran-modified buffer was perfused over the cells during and after the cell stimulation. vWF strings were counted at a position 2 mm downstream of the center of the electrode in each frame during and following heating. The ECM of the EC was isolated by perfusing 0.1 mM ammonium hydroxide in complete media over the EC for 30 min. The remaining ECM was fixed with 2% glutaraldehyde and blocked with 5% BSA for 1 h at 20 °C. The cells were then incubated with a primary anti-laminin and anti-collagen I, or, anti-fibronectin and anti-collagen IV (1 : 500, 0.01% Triton™ X-100 and 1% BSA in PBS) for 90 min at room temperature and labeled with a goat anti-rabbit IgG H&L antibody and a goat anti-mouse IgG H&L antibody (40 μg mL^{-1}, 1% BSA in PBS) for 60 min.

Whole blood flow assays

HUVEC-seeded microfluidic channels were transferred onto glass slides containing the patterned and insulated electrode (ESI,† Fig. S1). Experiments were performed in a heated microscope incubator at 37 °C and 5% CO_2 (INUG2A ZILCS, Tokai Hit). After allowing for temperature equilibration of the device and electrode for 10 min, voltage (5–9 V) was applied for 30 s either during whole blood perfusion or 2 min prior to whole blood perfusion. In the experiments where heat was applied during the blood perfusion, blood was perfused through the channel for 30 s prior to heating, the voltage was then applied for 30 s while the blood was flowing and for 6 min after the heating was stopped. In experiments where heat was applied prior to perfusion, 6.25% dextran modified complete media was withdrawn at 15 μL min^{-1} using a syringe pump (PHD 2000, Harvard Apparatus) during and 1 min after the applied voltage. Next, whole blood was perfused at flow rate of 15 μL min^{-1} or 100 μL min^{-1}, corresponding to a wall shear rates of 150 and 1000 s^{-1}, for 7 min. For 1000 s^{-1}, the flow was ramped using a programmable syringe pump from 5 to 100 μL min^{-1} over 1 min to avoid EC sloughing off the surface.

Measurement of platelet accumulation on ECM proteins

Fibronectin (100 μg mL^{-1}), laminin (100 μg mL^{-1}) or a 1 : 1 mixture of the proteins (50 μg mL^{-1} : 50 μg mL^{-1}) were incubated on clean glass slides in FAST frame multislide plate containing incubation chambers (Whatman, GE Healthcare Sciences) for 1 h.[25,26] Next, whole blood collected into PPACK was perfused over the prepared protein patches (5 mm × 5 mm) at flow rate of 15 μL min^{-1} (150 s^{-1}) for 7 min. Controls were conducted to determine the effect of heating on the ECM proteins. Fibronectin (100 μg mL^{-1}) or a 1 : 1 mixture of fibronectin/laminin (50 μg mL^{-1} : 50 μg mL^{-1}) were incubated inside the microfluidic channels for 1 h. We applied 7 V in fibronectin and laminin/fibronectin coated channels while flowing buffer at 150 s^{-1} for 30 s. After 1 min of cooling, whole blood collected into PPACK was perfused over the heat-treated proteins for at a flow rate of 15 μL min^{-1} (150 s^{-1}) for 7 min.

Image analysis

Transient platelet accumulation was monitored using an inverted microscope (IX81, Olympus, Center Valley, PA) with a 20× objective (NA 0.45) and Hoffman modulation optics. The microscope was outfitted with a motorized stage (Proscan, Prior Scientific, Rockland, MA), 16-bit CCD camera (Orca-ER, Hamamastu) controlled by Slidebook 5.0 software (Intelligent Imaging Innovations, Denver, CO). Data was collected at 15 frames per minute. Immediately following the perfusion of the whole blood, complete media was perfused through the device for 2 min to rinse out non-adherent blood cells. Adhered cells were then fixed with 2% glutaraldehyde in PBS for 2 min. EC were rinsed with PBS, permeabilized with 0.2% Triton™ X-100 detergent for 10 min, rinsed with PBS and labeled with FITC-phalloidin and DAPI for 1 h at room temperature. Fixed platelet aggregates and endothelial cells were imaged by confocal microscopy at 250 μm intervals up- and downstream of the electrode. Total platelet aggregate volumes were measured using the *z*-stack function on the confocal microscope with a 1 μm slice height. The Stack Tool in ImageJ (NIH, Bethesda, MD) was used to threshold three-dimensional reconstructions and calculate volumes.

Theoretical model of heat transfer

The change in temperature within the HUVEC coated channel caused by the heat flux from resistive heating of the microelectrode was estimated using finite element method software (COMSOL, Burlington, MA). Two models were developed; (1) a model of the bare electrode to compare with infrared camera measurements (ESI,† Fig S3A), and (2) a model of the PDMS device on top of the electrode to make estimates of temperature profiles in EC-coated channels (ESI,† Fig. S3B). Each model used the exact dimensions of the device. In Model 1, the two-dimensional transient conservation of energy equation was solved:

$$\rho_{\mathrm{i}} C_{\mathrm{p,i}} \frac{\partial T}{\partial t} = \vec{\nabla} \cdot \left(k_{\mathrm{i}} \vec{\nabla} T \right) + Q \tag{1}$$

where i denotes the material, T is the temperature, t is time, ρ_{i} is the material density, $C_{\mathrm{p,i}}$ is the material heat capacity, and k_{i} is the material thermal conductivity. Q is the heat source that was set to zero for all materials except for the gold. The heat source was modeled as a 30 s rectangular square wave of voltage and the power density was calculated at each voltage by:

$$P_{\mathrm{v}} = \frac{V^2}{\rho L^2} \tag{2}$$

where P_{v} is the power density, V is the voltage, ρ is the bulk resistivity of gold (24 nΩ m^{-1}), and L is the length of the electrode. Table 1 shows the materials and thermal properties used in the model.

Model 2 includes heat dissipation by conduction through the bordering solids (eqn 1) and by convection within the liquid. For the liquid phase the transient conservation of energy equation is:

$$\rho_{\mathrm{i}} C_{\mathrm{p,i}} \frac{\partial T}{\partial t} + \rho_{\mathrm{i}} C_{\mathrm{p,i}} \vec{v} \cdot \vec{\nabla} T = \vec{\nabla} \cdot \left(k_{\mathrm{i}} \vec{\nabla} T \right) + Q \tag{3}$$

Table 1 Thermophysical material properties and thicknesses used in computational models

Material	Heat capacity at constant pressure ($\mathrm{J\ kg^{-1}\ K^{-1}}$)	Density ($\mathrm{kg\ m^{-3}}$)	Conductivity ($\mathrm{W\ m^{-1}\ K^{-1}}$)	Thickness
Silica Glass[47]	710	2240	1.05	1.2 mm
Gold[47]	129	19 300	320	85 nm
Photoresist[48]	1200	1190	0.2	1 μm
Bottom PDMS[49]	1500	970	0.15	45 μm
Blood[50]	3620	1060	0.52	100 μm
Water/EC[51]	4180	1000	0.58	2 μm
Top PDMS[49]	1500	970	0.15	7.5 cm

The velocity (v) was defined as:

$$\vec{v} = 1.5U\left(1 - \frac{4y^2}{h^2}\right) \tag{4}$$

where p is the gradient of pressure, μ is the dynamic viscosity. The average velocity (U) was 2.5×10^{-3} m $\mathrm{s^{-1}}$.

For both models, the boundary condition at all surfaces except for the bottom surface was free convection with air:

$$-\vec{n} \cdot \left(-k \vec{\nabla} T \right) = h \cdot (T_{\mathrm{ext}} - T) \tag{5}$$

where T_{ext} is 37 °C and the heat transfer coefficient was calculated from the simplified convection formula over a flat plate:[27]

$$h = C\left(\frac{T_{\mathrm{S}} - T_{\mathrm{ext}}}{L}\right)^n \tag{6}$$

where h is overall heat transfer coefficient, T_{s} is the surface temperature which varies over the surface, T_{ext} is the ambient temperature, L is characteristic length (1.45 mm), and C and n are constants defined as 1.32 and 0.25, respectively. A Neumann boundary condition was used at the bottom of the glass slide:

$$-\vec{n} \cdot \left(-k \vec{\nabla} T \right) = q \tag{7}$$

where q is the heat flux ($\mathrm{W\ m^{-2}}$) from the microelectrode glass slide to the glass surface underneath. Mesh independence was confirmed by achieving temperatures within a 5% difference between 6734–34 909 elements in Model 1 and 18 521–159 706 elements in Model 2.

Statistical procedures

Data are presented as a mean ± the standard error of the mean of 3–5 donors for each experimental condition. Differences in platelet volumes were compared using the Mann–Whitney *U*-test. A p-value of less than 0.01 was considered statistically significant. Calculations were conducted using Prism 5 (GraphPad Software, Inc., La Jolla, CA). The goodness-of-fit of the COMSOL model to the experimental data was obtained in Matlab (version 2013b, Mathworks, Natick, MA) using the normalized mean square error.

Results

Electrode characterization

The temperature distribution resulting from resistive heating of the microelectrodes was measured and modeled as a function of voltage. Fig. 1A and B show the temperature distribution on and around insulated microelectrodes without the PDMS device. Applying potential of 5–9 V for 30 s produced peak temperature increases of 20–70 °C as measured with a thermal imaging camera. The goodness-of-fit between Model 1 (ESI,† Fig. S3A) and the experimental results was greater than 0.9 for each voltage (Fig. 1A). These results show that the Model 1 predicts accurate heat fluxes due to resistive heating in the microelectrode. As expected, in the absence of forced convection the peak temperature is centered over the electrode and decreases symmetrically in the *x*-direction (Fig. 1B).

Model 2 expands Model 1 to include fluid flowing through an endothelialized PDMS channel placed on top of the microelectrode (ESI,† Fig. S3B). The higher heat dissipation due to forced convection and additional conductive resistances of the cells reduced the peak temperatures at the cell–buffer interface (2 μm above the bottom PDMS channel) compared to Model 1. The computational model predicts a temperature increased of 10–40 °C experienced by the EC for potentials of 5–9 V (Fig. 1C). The peak temperature rise is a linear function of voltage (r^2 = 0.99). At 30 s, when peak temperature was reached, the temperature in the flow direction increased rapidly upstream of the electrode. The highest temperature occurs at the downstream edge (x = 750 μm) of the electrode (Fig. 1D). The temperature was skewed downstream of the electrode due to heat transfer by forced convection.

Viability of EC and activation following heating

PDMS microfluidic channels with confluent EC monolayers were placed over the electrodes (ESI,† Fig. S2). Dextran modified complete media was perfused through the channels at a wall shear rate of 150 s^{-1} while a 5–9 V potential was applied for 30 s. Following two additional minutes of buffer perfusion, cells were fixed and stained for viability (ethidium bromide), P-selectin, and phosphatidylserine (PS) exposure (annexin V). At 5 and 6 V, little to no P-selectin expression and cell death was observed (Fig. 2, 5 V data not shown). At 7 V, dead cells were found between 0.5 mm upstream to 1.8 mm downstream of the center of the electrode. PS exposure showed a similar distribution as dead cells (ESI,† Fig. S4). P-selectin positive EC, covered an area extending from 1.0 mm upstream of the center of electrode to 3.5 mm downstream of the electrode. At 8 V, dead cells were found from 1.0 mm upstream to 3.5 mm downstream of the center of the electrode (Fig. 2A). P-selectin positive EC spanned 1.5 mm upstream of the injury zone to 4 mm downstream of injury center (Fig. 2B). The distribution of dead and activated EC skews downstream, which is congruent with the predicted temperature distribution by Model 2 (Fig. 1D).

Moderate heating leads to retraction of EC that reveals a protein-rich matrix

The contact between the EC were lost and gaps between EC increased in a voltage-dependent manner. There were no

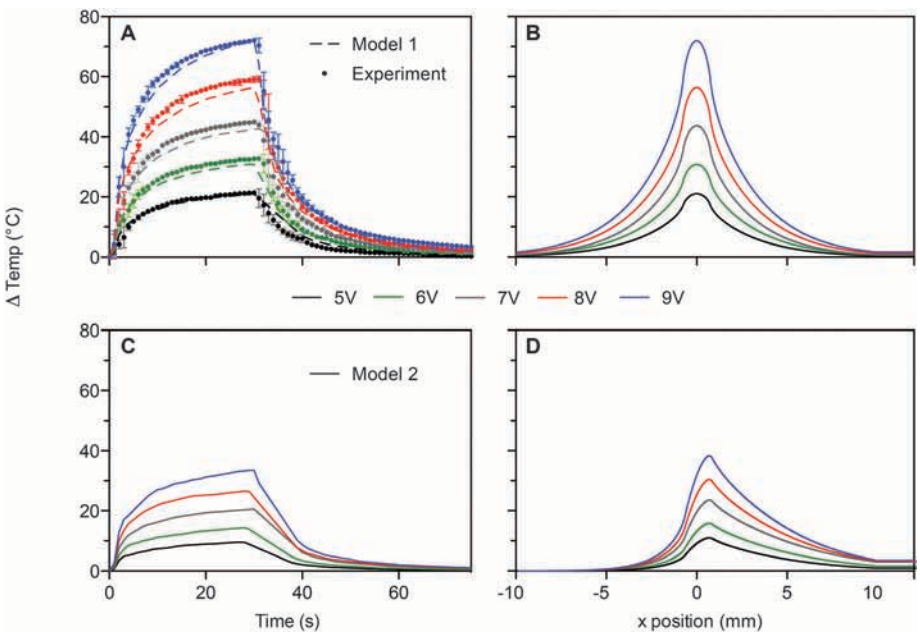

Fig. 1 Electrode temperature measurements. (A) The change in surface temperature at the middle of the electrode (x = 0) as a function of voltage for a 40 μm PDMS thick film atop the microelectrode measured using a thermal camera. Model 1 was used to simulate the same conditions to validate heat flux predictions from resistive heating in the electrode. (B) Temperature distribution along the wall of the PDMS film predicted by Model 1 for the same conditions as (A) at t = 30 s. (C) Transient temperature change over the top of the electrode as predicted by Model 2 for the assembled device at a wall shear rate of 150 s^{-1}. The temperature over time is reported at the center of the electrode at the cell–buffer interface. (D) Temperature distribution along the surface of the EC monolayer predicted by Model 2 from the same conditions used in (C) at t = 30 s.

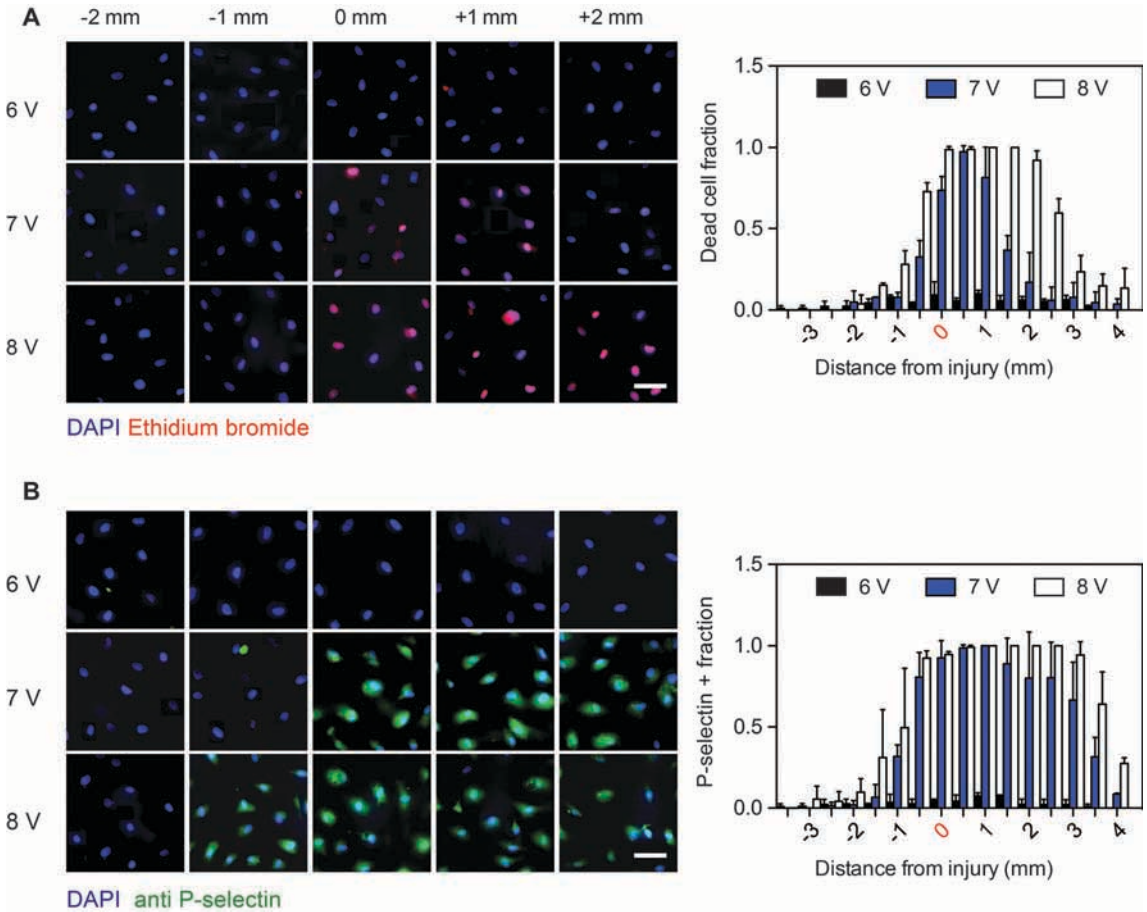

Fig. 2 Viability and P-selectin expression of EC following heating. Representative images and fraction of dead cells (A) and P-selectin positive cells (B) following heating by 6, 7 and 8 V for 30 seconds. Scale bar = 50 μm. Red number (x = 0) indicates the center of the electrode. The electrode spans the distance from −725 to +725 μm. Negative numbers are upstream of the electrode and positive numbers are downstream of the electrode.

apparent gaps between EC at 5 and 6 V. A potential of 6.5 V yielded a 30% decrease in EC area directly over the electrode and observed gaps up to 2.5 mm downstream of the electrode (Fig. 3A and B). A potential of 7 V lead to large gaps up- and downstream, but very small gaps directly over the electrode (Fig. 3C and D). Similarly, a potential of 8 V led to small gaps near the electrode with the largest gaps present 2.5–3.7 mm downstream (Fig. 3E and F). These data suggest that a moderate amount of heating cause EC to lose their tight junctions and retract, but that above a certain temperature retraction is reduced or EC do not retract before losing viability. The exposed matrix under receded EC was rich in laminin, collagen IV and fibronectin with only a modest amount of collagen I (Fig. 4).

EC secrete and release vWF strands following heating

After applying voltage, the presence of vWF strings on EC was measured along the length of the channel (Fig. 5A). Approximately 10% of EC secreted vWF strings even far upstream (x = −3 mm) of the electrode where we expect no heating (Fig. 5B). In regions where heating is predicted to be highest (Fig. 1B), 1 mm upstream to 3 mm downstream of the electrode, there were three-fold as many vWF strings compared to unheated regions. The release of vWF increased with increasing voltage; 88 ± 9 vWF strings were released at 8 V compared to 25 ± 9 vWF strings at 6 V (Fig. 5C).

Simultaneous heat injury and whole blood perfusion

PPACK anticoagulated whole blood was perfused over EC during the 30 s voltage pulse and for 6 min afterwards at 150 s^{-1}. At 5–6 V, few platelets adhered to the surface, and few aggregates formed. At 7 V, we observed significant platelet accumulation with volumes of 45 000 ± 11 000 μm^3 at the downstream edge of the electrode (Fig. 6A and ESI,† Fig S5A). Most aggregates were observed from the center of the electrode to 1.5 mm downstream. At 8 V, platelet aggregate volumes were five-fold larger, 220 000 ± 35 000 μm^3, than aggregates formed at 7 V and found primarily downstream of the electrode (Fig. 6B).

Computational Model 2 predicts heating of not only the ECs, but penetration of heat across the height of the channel. There was only a 6% difference in peak temperatures between the bottom and top of the channel at x = 0 (ESI,† Fig. S6). We measured platelet adhesion to fibronectin coated channels in the absence of ECs at 5, 6, 7 and 8 V and a wall shear rate of 150 s^{-1} (ESI,† Fig S7) to test the effect of heating in the absence of EC. There was no platelet adhesion at 5 V and minor

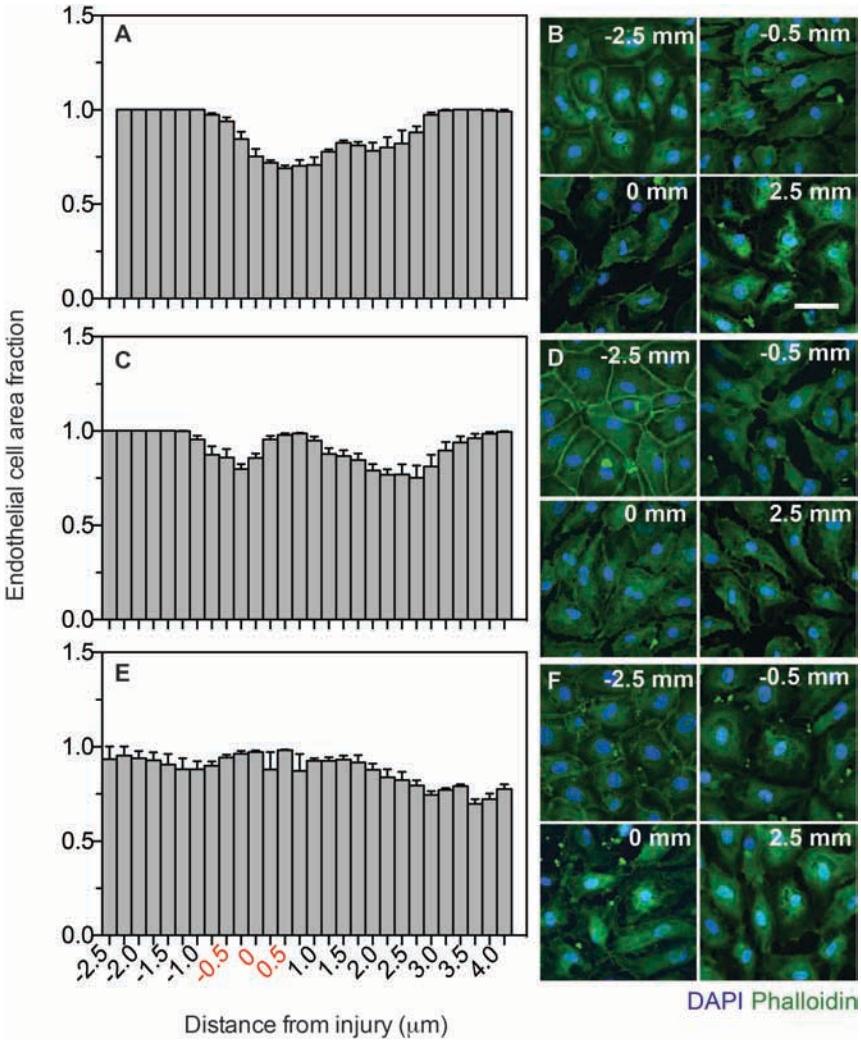

Fig. 3 Moderate heating leads to gaps between EC. Recession of EC following heating at different positions for 6.5, 7, and 8 V (A, C, E). Scale bar = 50 μm. EC area fraction was measured with the actin stain FITC-phalloidin (B, D, F). Red numbers (x = 0) indicate the center of the electrode. The electrode spans the distance from −725 to +725 μm.

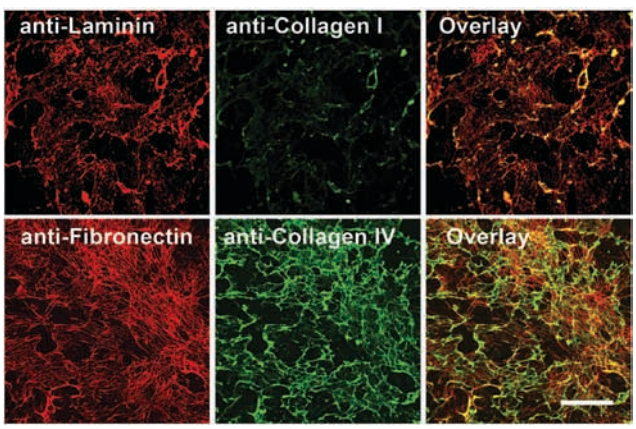

Fig. 4 HUVEC secrete a protein-rich matrix. Removal of EC and immunostaining reveals laminin, collagen IV, fibronectin, and collagen I in the extracellular matrix. Scale bar = 50 μm.

adhesion at 6 V (ESI,† Fig S7A). However, significant platelet aggregation was observed at 7 and 8 V, suggesting that the temperature increases experienced by platelets was enough to activate them (ESI,† Fig. S7B and C). At 7 V, there was a downstream shift in the distribution of the platelet aggregates (ESI,† Fig. S7B), perhaps due to a lag time between heating and activation. Similarly, significant platelet adhesion and aggregation was also measured in a BSA coated channel exposed to 7 V (ESI,† Fig. S7D). In any case, these data indicate that it would be difficult to decouple platelet accumulation due to EC activation and exposure of the subendothelial matrix from heat-induced platelet activation and adhesion in this model.

Whole blood perfusion following heat injury

To eliminate the influence of temperature on platelets, we heated under conditions that induced gaps between EC (6.5–8 V, Fig. 3) for 30 s while perfusing buffer through the channel followed by a 1 min cooling period and then a perfusion of whole blood for

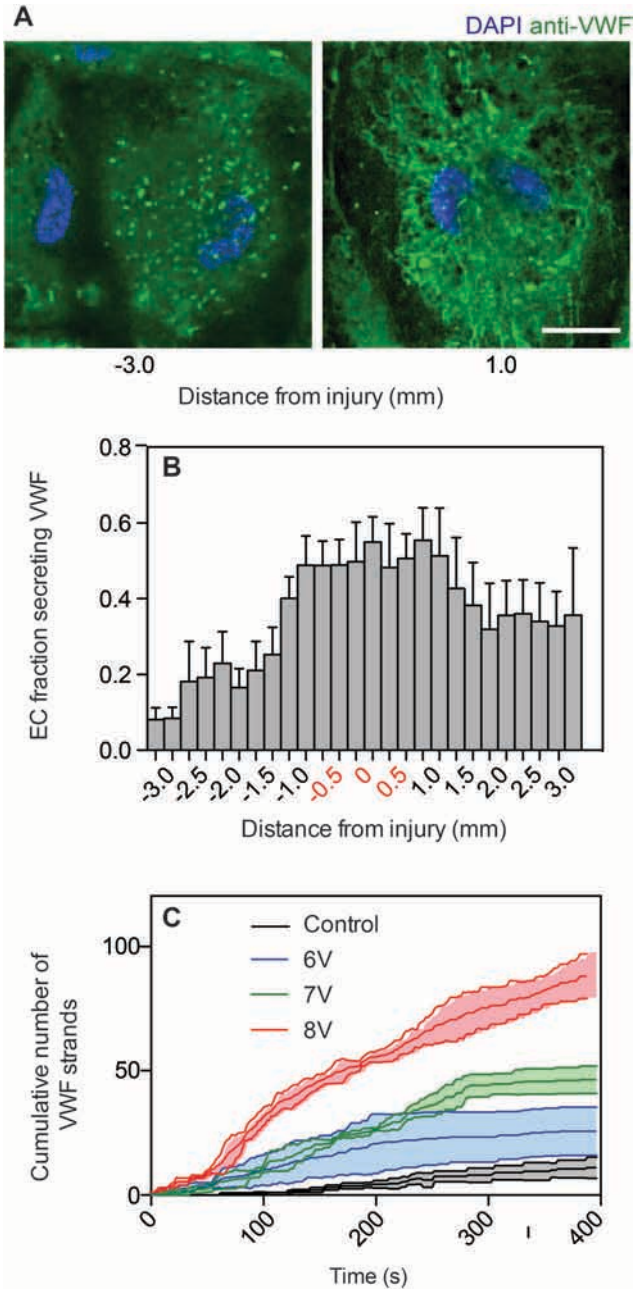

Fig. 5 vWF secretion following heat injury. (A) vWF is contained within Weibel–Palade bodies 3 mm upstream of the electrode and secreted into strings at 1 mm downstream of the electrode following 30 s heating (7 V) and 4 min perfusion at 150 s^{-1}. Scale bar = 20 μm. (B) Fraction of EC secreting vWF relative to the electrode position (n = 3–10). (C) The cumulative number of vWF strands released over time following heating by 0, 6, 7, and 8 V. The voltage was applied at 15 s.

7 min. At 6.5 V, corresponding to a predicted peak temperature increase of 19 °C, platelets accumulate directly over the electrode and downstream of the electrode with a skewed distribution (Fig. 7A and B). Platelet volumes reached a maximum size of 11 700 ± 5000 μm^3. At 7 V, which had a peak temperature increase of 22 °C, the distribution was bimodal with peaks of platelet accumulation 1.5 mm upstream and 1.5 mm downstream of the electrode injury (Fig. 7C and D). The upstream peak had aggregates that reached 4700 ± 1000 μm^3 while platelet aggregates reached 10 400 ± 1700 μm^3 downstream of the electrode. Directly over the electrode there was little platelet accumulation. A similar trend was observed at 8 V, with a peak in platelet accumulation 1.5 mm upstream of the electrode and more substantial platelet accumulation 2–4 mm downstream. Peak volumes of the platelets reached 3900 ± 1000 μm^3 upstream of the injury and 13 100 ± 2500 μm^3 downstream of the injury (Fig. 7E and F). Platelet adhesion correlated with the predicted temperature found at a give position for each voltage. For example, accumulation was found at predicted temperature increases of 16–22 °C. Changes in predicted temperature increases exceeding 23 °C resulted in EC death and little to no platelet accumulation. At 7 and 8 V the EC directly over the electrode had little recession and almost no platelet accumulation (Fig. 7C and E). Downstream of the electrode at 7 V, large gaps between ECs and significant platelet accumulation in these gaps was observed (Fig. 7C).

Real-time measurement of platelet accumulation show platelet aggregates grow for the first 2–3 min of the assay on top of and between EC, followed by some shedding of loosely adhered platelets and platelet aggregates on top of EC (ESI,† Fig. S8). Firm platelet aggregates only remained in the retracted spaces between P-selectin positive EC.

At 7 V, whole blood perfusion at 1000 s^{-1} showed similar aggregate volumes as at 150 s^{-1} (ESI,† Fig. S9). A bimodal distribution had peak volumes of 4600 ± 1800 μm^3 upstream of the electrode and 8600 ± 1900 μm^3 downstream of the electrode. These data show that the model can support platelet adhesion at both venous and arterial shear rates, but that the final volume of platelet aggregates is not strongly dependent on shear rate.

Platelet adhesion between heat activated EC is mediated by GPIbα and $\alpha_6\beta_1$ receptors

During the flow assay, platelets rolled on EC, but permanent deposition was only observed in the gaps between EC. Because vWF strings were released by heat-activated EC (Fig. 5), we expected that platelet adhesion is at least partially supported by GPIbα–vWF interactions. Indeed, inhibition of GPIbα resulted in a three-fold reduction in peak platelet aggregate volume over the electrode on EC stimulated by 6.5 V (Fig. 8A). EC secrete laminin[28] and we found that in this model the matrix beneath EC was laminin-rich (Fig. 4). Platelets can firmly adhere on laminin through the integrin $\alpha_6\beta_1$ at venous shear rates as used in these experiments.[29] In the presence of an anti-α_6 function-blocking antibody there was a dramatic reduction in platelet accumulation and almost no visible aggregation (Fig. 8). Inhibition of $\alpha_{IIb}\beta_3$ was a negative control that resulted in no aggregation and only individual platelets adhered between the EC (Fig. 8). Combining anti-$\alpha_6\beta_1$ with either anti-$\alpha_{IIb}\beta_3$ or anti-GPIbα lead to near complete inhibition of platelet adhesion (Fig. 8A and B).

To compare the EC secreted extracellular matrix to purified proteins, platelets were perfused over surfaces of laminin and fibronectin and a 1 : 1 mixture of both. These proteins were chosen because fibronectin is used for seeding EC and laminin is abundent in the ECM (Fig. 4). Collagen IV is also abundant, but platelets do not express any known receptors for collagen IV. A mean

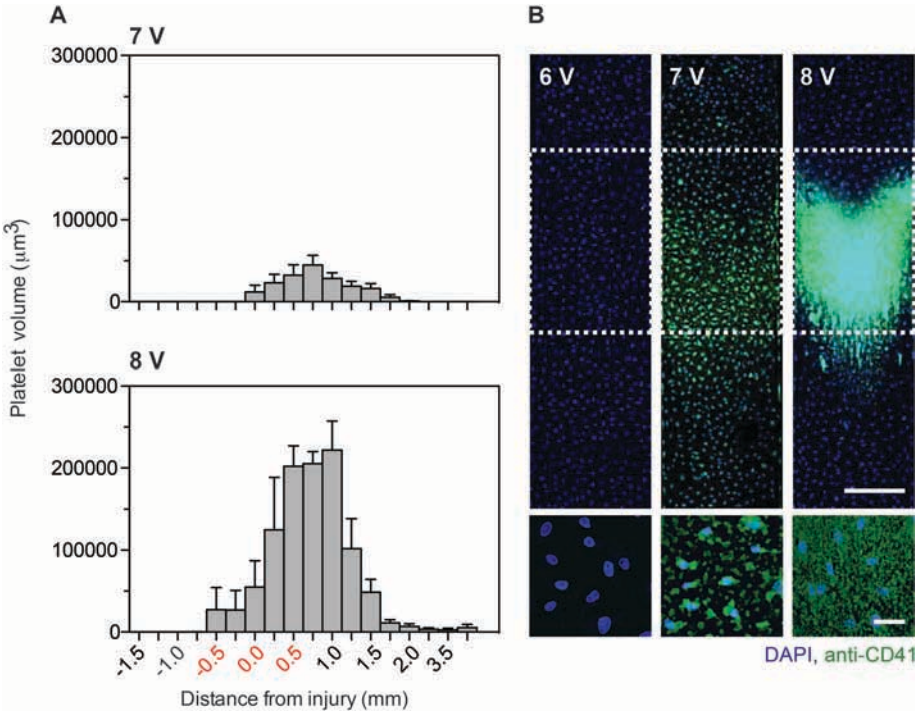

Fig. 6 Simultaneous heat injury and whole blood perfusion. (A) Platelet accumulation on EC heated by 7 V and 8 V for 30 s followed by 6 min of whole blood perfusion at 150 s^{-1}. Red numbers indicate locations directly over the gold electrode. The electrode ranges from −725 to +725 μm. (B) Platelet accumulation (green) along the channel near the electrode and a zoomed in view at x = 1 mm. EC labeled with DAPI (blue). White dotted lines indicated the location of the electrode. Channel image: scale bar = 500 μm. Zoomed in image: scale bar = 50 μm.

platelet volume of 73 900 μm^3 accumulated over a 1 : 1 mixture of laminin and fibronectin (ESI,† Fig. S10). Mean volumes of 1160 μm^3 and 22 000 μm^3 were measured on fibronectin and laminin, respectively. These conditions were compared to platelet aggregate volumes obtained on heat-treated EC at the position of the maximum size (Fig. 7). Platelet aggregate volumes were normalized by the area available for adhesion (Table 2). The normalized platelet aggregate volumes in the EC injury model at 6.5, 7, and 8 V were 1.04 μm^3 μm^{-2}, 1.00 μm^3 μm^{-2}, and 1.12 μm^3 μm^{-2}, respectively. These volumes are less than the purified 1 : 1 laminin:fibronectin surface (1.65 μm^3 μm^{-2}), but more than laminin alone (0.49 μm^3 μm^{-2}).

Excessive heating of ECM proteins can alter their adhesive properties. Applying 7 V for 30 s to a mixed laminin–fibronectin surface, but not fibronectin alone, resulted in diminished platelet adhesion at the hottest predicted position of the channel, directly downstream of the electrode (ESI,† Fig. S11). There was little to no platelet adhesion at this same position in the presence of EC (Fig. 7). In simultaneous heat injury and blood perfusion experiments, maximum platelet accumulation occurred at this position suggesting platelet activation and integration was an artifact of heating (Fig. 6).

Correlating EC activation, viability and platelet accumulation with temperature

Fig. 9A shows a heat map of the predicted temperature increase from Model 2, dead cell fraction, P-selectin and annexin V positive EC, vWF secretion, degree of EC recession, and platelet accumulation at different positions for a 7 V heat injury prior to blood flow. The highest predicted temperatures correlate with the highest fraction of dead cells. The most P-selectin positive EC were found on dead cells, but there is also considerable expression on viable cells, that experience significant heating. Measurable vWF strings were present in the entire channel, but were elevated between 0.5 mm upstream and 3.0 mm downstream of the channel, similar to the distribution of P-selectin. In the downstream region of 1.5–3.0 mm, EC were viable, vWF secreting, and mostly P-selectin positive. It is in this region where EC retraction and platelet accumulation was most prominent (Fig. 9B). PS exposure as measured by annexin V expression was primarily found to overlap with the dead cells, however some viable and activated EC may also support PS-mediated coagulation reactions. Based on these data we define three distinct zones: (1) A kill zone that occurs above a certain temperature where there is little EC recession and platelet accumulation. (2) An activation zone characterized by the presence of P-selectin positive and viable EC where EC retract providing a vWF and laminin-rich surface for platelets adhesion. (3) A quiescent zone where EC are viable and not activated that does not promote platelet adhesion.

Discussion

The objective of this study was to develop an *in vitro* focal injury model in which an area of activated EC that would promote platelet adhesion was surrounded by an area of quiescent EC that would inhibit platelet activation. We used resistive heating

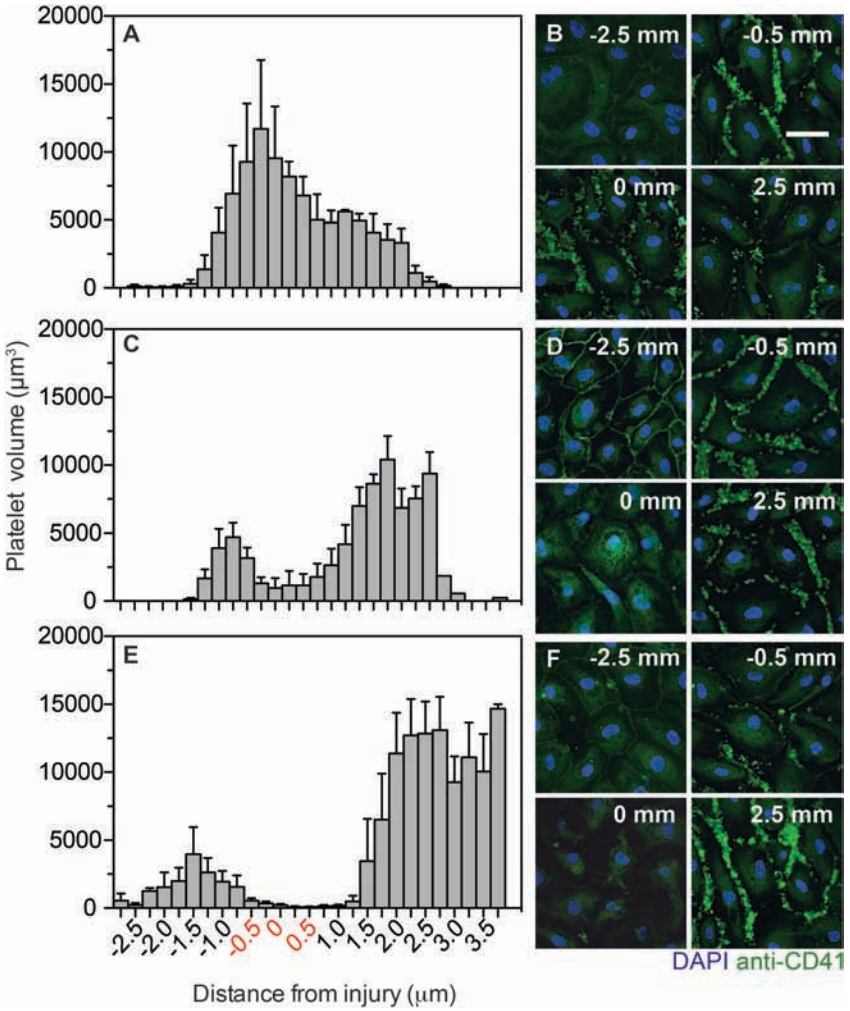

Fig. 7 Whole blood perfusion following heat injury. Platelet volumes and representative images of platelet accumulation at 150 s^{-1} following heating by 6.5 (A, B), 7 (C, D) and 8 (E, F) V for 30 s. Red numbers indicate locations directly over the gold electrode. The electrode ranges from −725 to +725 μm. Scale bar = 50 μm.

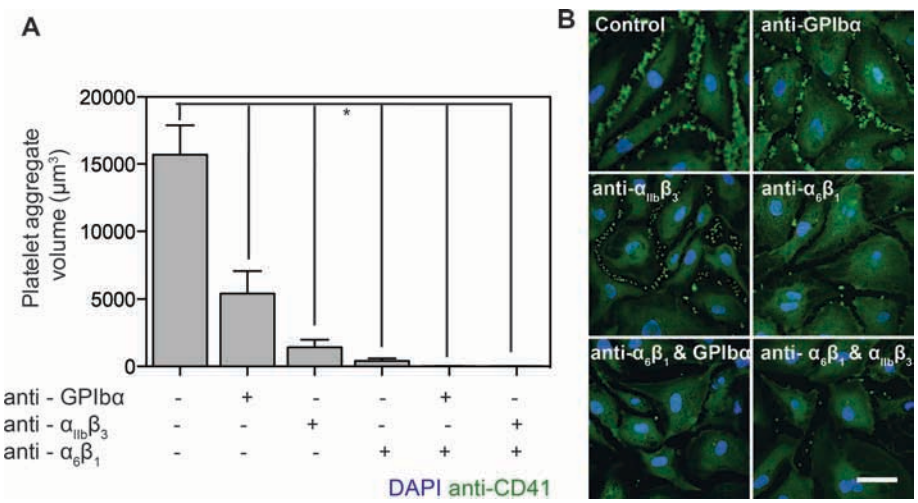

Fig. 8 Platelet adhesion between heat activated EC is mediated by GPIbα and $\alpha_6\beta_1$ receptors. (A) Platelet aggregate volumes over the electrode following perfusion of EC heated by 6.5 V for 30 s in the presence of anti-GPIbα, abciximab (anti-$\alpha_{IIb}\beta_3$), and anti-$\alpha_6\beta_1$ antibodies. Error bars indicate standard error of the mean across donors at each condition. Significant differences ($p < 0.01$) denoted by *. (B) Representative images of platelet adhesion in presence of blocking antibodies. Scale bar = 30 μm.

Table 2 Platelet aggregate volumes on purified protein and heat-injured EC surfaces. The mean volumes for the heat-injured EC are obtained from the location of the maximum platelet volume at each voltage. The corresponding mean area and area fraction of exposed ECM at each location is reported. The mean volume is divided by the mean area of the ECM available for adhesion to obtain the normalized mean volume

Surface	Mean volume (μm^3)	Mean area of exposed ECM (μm^2) (area fraction)	Normalized mean volume ($\mu m^3\ \mu m^{-2}$)
Fibronectin	1160	44 900 (1)	2.58×10^{-2}
Laminin	22 000	44 900 (1)	4.90×10^{-1}
Laminin and fibronectin	73 900	44 900 (1)	1.65
Injury at 6.5 V	11 700	11 200 (0.25)	1.04
Injury at 7 V	10 400	10 300 (0.23)	1.00
Injury at 8 V	13 100	11 700 (0.26)	1.12

of a surface microelectrode to provide a heat source to focally stimulate cultured EC in microfluidic channels. Computational models were developed to aid in the interpretation of experimental results and predict the temperature distribution as a function of flow conditions and applied potential. We used EC activation markers, EC recession, and viability to characterize the response of EC to elevated temperatures. Whole blood flow assays showed that millimeter-scale EC activation zones could be achieved that supported firm platelet adhesion and aggregation, primarily through GPIbα and $\alpha_6\beta_1$ receptors.

Predicted heating from computational models were correlated to different zones of EC activation and platelet accumulation. A kill zone corresponded to peak temperature increases of greater than 23 °C characterized by EC death, elevated levels of P-selectin, PS exposure and vWF secretions, but did not support platelet adhesion. An activation zone corresponded to peak temperature increases of 16–22 °C characterized by viable EC, elevated levels of P-selectin and vWF, significant recession of EC, exposure of the underlying extracellular matrix, and robust platelet adhesion and aggregation. A quiescent zone corresponded to peak temperature increases of less than 15 °C characterized by EC that were viable, did not show an increase in P-selectin or vWF secretion compared to unheated cells, and did not support platelet adhesion. The transition between the kill zone and activated zone is apparently quite sensitive to

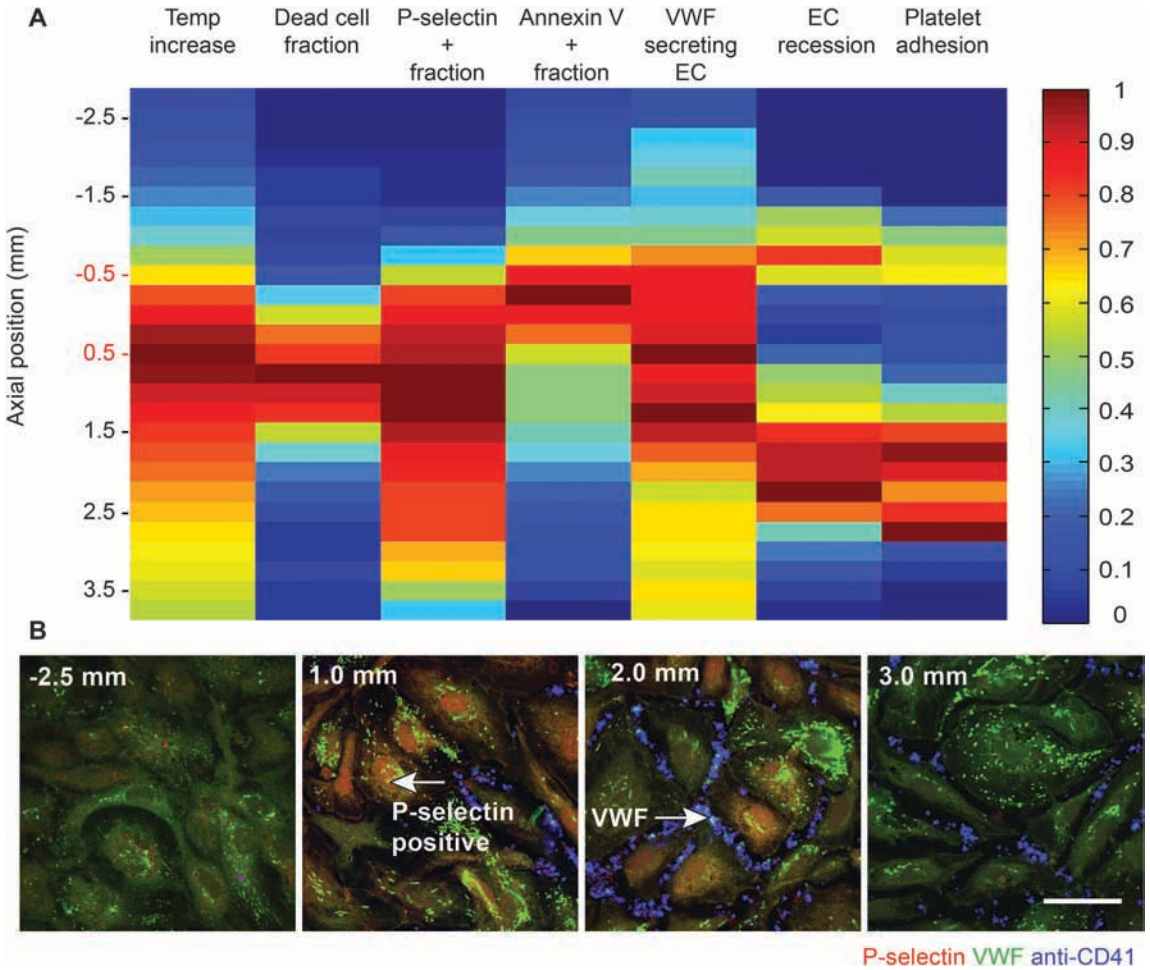

Fig. 9 Correlating EC activation, viability and platelet accumulation with temperature. (A) A heat map compares the predicted temperature from Model 2, fraction of dead cell fraction, fraction of P-selectin and annexin V positive (+) cells, vWF secretion, EC recession and platelet accumulation (after heating) as a function of position for EC heated by 7 V for 30 s. Each parameter was normalized by the largest value in the data set. Red text indicates the position of the electrode. (B) Representative images show the overlay of P-selectin, vWF and platelets overlaid. Scale bar=50 μm.

temperature since we observed little activation at 6 V (predicted temperature = 15 °C) over the electrode and significant levels of cell death at 7 V (predicted temperature = 23 °C) and 8 V (predicted temperature = 30 °C). At 6.5 V (predicted temperature = 19 °C) we were able to focally activate EC and promote platelet adhesion without significant cell death. The transitions between these phenotypes were not sharp, but rather follow the gradients in predicted surface temperature.

Observations in this injury model were consistent with other *in vitro* and *in vivo* injury models of heat-induced cell injury. In a baboon heat stroke model, exposure to environmental heat stress until a core temperature of 42.5 °C was attained caused widening of gaps between the EC, increased content release of the Weibel Palade bodies, tissue factor exposure, and endothelial cell–platelet interactions.[30] Many of these features were also observed in our microelectrode heating model. Other *in vitro* models have shown cell death after hyperthermia, as we observed at peak temperature changes greater than 23 °C. For example, murine mastocytomas subjected to temperature increases 42–47 °C have accelerated apoptosis and necrosis as the thermal dose is increased.[31]

In our model, platelet accumulation was completely abolished directly over the electrode at 7 and 8 V, which corresponded to 23–40 °C temperature increases in our computational model. As was shown in our control experiments performed with ECM proteins, platelet adhesion was not supported just downstream of the electrode after 7 V had been applied. Bos *et al.* also demonstrated decreased platelet adhesion to thermally injured subendothelium after 15 s of exposure to elevated temperatures, which was largely attributed to denaturation of vWF.[32] Decreases of 25%, 50% and 75% platelet accumulation on the ECM were found to occur at temperatures increases of ~32, 35 and 38 °C.

Heat-induced EC activation recreates some features reported in laser injury models of thrombosis. The matrix proteins that are exposed in this model depend on the degree of the injury. Moderate laser power can yield superficial vessel injuries in which the EC layer is denuded, exposing the subendothelial matrix, without significant exposure of the vessel wall.[33] In this case, platelet adhesion is mediated primarily by laminin, vWF, and type IV collagen, all of which are present in the ECM exposed in our heat injury model. Importantly, the data presented here show ECM proteins and platelet adhesion are significantly influenced by even modest temperature changes. Therefore, laser intensities that either alter the structure of ECM proteins or directly heat platelets, could influence initial platelet adhesion in these models.

Heat-induced EC activation recreates aspects of chemical injuries induced by calcium ionophores or staurosporine. Staurosporine, a nonspecific protein kinase inhibitor, causes EC to undergo apoptosis and support platelet adhesion.[34,35] High temperatures in our heat injury model lead to EC death and exposure of PS. However, these areas to do not support platelet adhesion, possibly due to denaturation of ECM proteins. Calcium ionophores can be used to induce secretion of Weibel–Palade bodies,[36] supporting transient platelet adhesion *via* GPIbα, but not firm adhesion and aggregation.[37] The combined release of Weibel–Palade bodies and EC recession were necessary for firm platelet adhesion in the heat injury model. A distinct advantage of our electrode heat injury over these chemical injuries is the spatial control of EC activation.

Platelet accumulation in the EC activation zone was mediated by GPIbα and $\alpha_6\beta_1$ receptors. Inhibition of GPIbα resulted in less rolling over EC, but platelets were still able to adhere in the gaps between receded EC. At the lower shear rates used in most of the experiments study (150 s^{-1}), GPIbα is not necessary for platelet adhesion, but likely aids platelet recruitment to the EC surface and aggregation through vWF. Previous *in vivo* and *in vitro* studies show a supporting role for GPIbα mediated adhesion and activation at low shear rates.[25,38,39] Platelet accumulation was also supported at a high shear rate (1000 s^{-1}) in the model, where vWF supported rolling is necessary for platelet adhesion. Interactions between the integrin $\alpha_6\beta_1$ and the extracellular matrix between EC were necessary for robust platelet adhesion and aggregation. Platelet adhesion to laminin is mediated by integrin $\alpha_6\beta_1$.[40] A 69% and 82% reduction in thrombus volume is reported in guidewire and moderate laser injury models, respectively, with an $\alpha_6^{-/-}$ mouse. These results are also supported by studies that demonstrate platelet adhesion and aggregation are dependent on synergistic interactions between $\alpha_{IIb}\beta_3$, $\alpha_6\beta_1$ and $\alpha_5\beta_1$ on the ECM of carotid arteries that have been dissected and ligated with a surgical filament to induce injury.[41]

Cumulative platelet accumulation and their spatial distribution were influenced by EC phenotype. Platelets firmly adhered and aggregated only in the gaps between the retracted EC. Moreover, platelet aggregate volumes were smaller in these gaps than on laminin–fibronectin surfaces. There was also little difference in platelet aggregates formed at average wall shear rates of 150 and 1000 s^{-1}, in contrast to *in vitro* flow assays on purified proteins.[42] These observations may be due to platelets favoring adhesion in the low shear stress valleys between EC or by secretion of platelet inhibitors such as NO.[43] We have previously shown the mass transfer limitations of NO inhibition of platelet aggregation as a function of shear rate using NO release from polymers.[44,45] Of note was the prediction that NO would only be an effective platelet inhibitor within tens of micrometers of an adhesive surface, which is the case for the gaps between EC in the activation zone in the heat-injury model presented here. Future studies are needed to determine the relative roles of rheology, transport and the pro- and anti-platelet mechanisms of EC on platelet accumulation as a function of injury size and this model may provide a valuable tool for exploring these interactions.

While temperature was not measured directly in microfluidic channels, we used a computational model to make predictions of the temperature distribution. Even if there were discrepancies between the model and experiment in the absolute temperature, the relative differences between applied potential were likely well predicted by the model since the temperature and applied voltage were linearly proportional. EC response to mechanical and oxidative stresses depends on both the magnitude and duration of the insult.[46] We would expect the same hold true for temperature, but here, we limited studies to a constant duration of heating of 30 s.

Simultaneous heating and whole blood perfusion caused platelet accumulation that was independent of receptor-mediated adhesion mechanisms. Future studies are needed to determine if heat pulses with shorter periods, but higher intensity, could provide EC activation without affecting platelet function.

Conclusion

We developed a focal vascular injury model in which EC are activated by resistive heating of surface microelectrodes. EC could be differentially activated or killed as a function of the temperature at the millimeter length scale. Here, a simple electrode with a fixed width was used, but the same fabrication procedure could be used to define smaller or larger electrodes, or a series of electrodes within a single channel to define multiple activation zones. This model provides a tool for studying platelet interactions with subendothelial matrices in the presence of activated EC surrounded by quiescent EC. This is in contrast to the majority of *in vitro* flow assays that use either purified proteins or activation of entire surfaces of EC. The juxtaposition of quiescent and activated EC allows for future studies related to relative roles of pro- and antithrombotic function of EC as function of injury size, shear stress and EC activation state.

Acknowledgements

This work was supported by NSF CAREER (CBET-1351672), American Heart Association (14GRNT20410094) and NIH (RO1HL120728, R21NS082933).

References

1 M. A. Gimbrone, *Ann. N. Y. Acad. Sci.*, 1987, **516**, 5–11.
2 P. S. Frenette, C. Moyna, D. W. Hartwell, J. B. Lowe, R. O. Hynes and D. D. Wagner, *Blood*, 1998, **91**, 1318–1324.
3 R. G. Mason, D. Sharp, H. Y. Chuang and S. F. Mohammad, *Arch. Pathol. Lab. Med.*, 1977, **101**, 61–64.
4 A. Kingsnorth and A. A. Majid, *Principles of Surgical Practice*, Cambridge University Press, 2001.
5 J. J. Zwaginga, G. Nash, M. R. King, J. W. M. Heemskerk, M. Frojmovic, M. F. Hoylaerts and K. S. Sakariassen, Biorheology Subcommittee of the SSC of the ISTH, *J. Thromb. Haemostasis*, 2006, **4**, 2486–2487.
6 J. J. Zwaginga, K. S. Sakariassen, G. Nash, M. R. King, J. W. Heemskerk, M. Frojmovic and M. F. Hoylaerts, Biorheology Subcommittee of the SSC of the ISTH, *J. Thromb. Haemostasis*, 2006, **4**, 2716–2717.
7 M. Roest, A. Reininger, J. J. Zwaginga, M. R. King and J. W. M. Heemskerk, The Biorheology Subcommittee of the SSC of the ISTH, *J. Thromb. Haemostasis*, 2011, **9**, 2322–2324.
8 J. Heemskerk, K. S. Sakariassen, J. J. Zwaginga, L. F. Brass, S. P. Jackson and R. W. Farndale, The Biorheology Subcommittee of the SSC of the ISTH, *J. Thromb. Haemostasis*, 2011, **9**, 856–858.
9 R. Van Kruchten, J. M. Cosemans and J. W. Heemskerk, *Platelets*, 2012, **23**, 229–242.
10 K. B. Neeves, O. J. T. McCarty, A. J. Reininger, M. Sugimoto and M. R. King, The Biorheology Subcommittee of the SSC of the ISTH, *J. Thromb. Haemostasis*, 2014, **12**, 418–420.
11 S. M. de Witt, F. Swieringa, R. Cavill, M. M. E. Lamers, R. Van Kruchten, T. Mastenbroek, C. Baaten, S. Coort, N. Pugh, A. Schulz, I. Scharrer, K. Jurk, B. Zieger, K. J. Clemetson, R. W. Farndale, J. W. M. Heemskerk and J. M. E. M. Cosemans, *Nat. Commun.*, 2014, **5**, 1–13.
12 B. T. Atkinson, R. Jasuja, V. M. Chen, P. Nandivada, B. Furie and B. C. Furie, *Blood*, 2010, **116**, 4675–4683.
13 J. J. Zwaginga, J. J. Sixma and P. G. de Groot, *Arterioscler., Thromb., Vasc. Biol.*, 1990, **10**, 49–61.
14 P. J. Sammak, L. E. Hinman, P. O. Tran, M. D. Sjaastad and T. E. Machen, *J. Cell Sci.*, 1997, **110**, 465–475.
15 A. Sagripantil and A. Carpi, *Biomed. Pharmacother.*, 2000, **54**, 107–111.
16 M. Tsai, A. Kita, J. Leach, R. Rounsevell, J. N. Huang, J. Moake, R. E. Ware, D. A. Fletcher and W. A. Lam, *J. Clin. Invest.*, 2012, **122**, 408–418.
17 Y. Zheng, J. Chen, M. Craven, N. W. Choi, S. Totorica, A. Diaz-Santana, P. Kermani, B. Hempstead, C. Fischbach-Teschl, J. A. Lopez and A. D. Stroock, *Proc. Natl. Acad. Sci. U. S. A.*, 2012, **109**, 9342–9347.
18 R. R. Hansen, A. R. Wufsus, S. T. Barton, A. A. Onasoga, R. M. Johnson-Paben and K. B. Neeves, *Ann. Biomed. Eng.*, 2012, **41**, 250–262.
19 F. Shen, C. J. Kastrup, Y. Liu and R. F. Ismagilov, *Arterioscler., Thromb., Vasc. Biol.*, 2008, **28**, 2035–2041.
20 C. J. Kastrup, F. Shen, M. K. Runyon and R. F. Ismagilov, *Biophys. J.*, 2007, **93**, 2969–2977.
21 A. A. Onasoga-Jarvis, T. J. Puls, S. K. O'Brien, L. Kuang, H. J. Liang and K. B. Neeves, *J. Thromb. Haemostasis*, 2013, **12**, 373–382.
22 U. M. Okorie, W. S. Denney, M. S. Chatterjee, K. B. Neeves and S. L. Diamond, *Blood*, 2008, **111**, 3507–3513.
23 J. C. McDonald, D. C. Duffy, J. R. Anderson, D. T. Chiu, H. K. Wu, O. Schueller and G. M. Whitesides, *Electrophoresis*, 2000, **21**, 27–40.
24 L. Rouleau, J. Rossi and R. L. Leask, *Ann. Biomed. Eng.*, 2010, **38**, 1451–1462.
25 K. B. Neeves, A. A. Onasoga, R. R. Hansen, J. J. Lilly, D. Venckunaite, M. B. Sumner, A. T. Irish, G. Brodsky, M. J. Manco-Johnson and J. A. Di Paola, *PLoS One*, 2013, **8**, 1–11.
26 R. R. Hansen, A. A. Tipnis, T. C. White-Adams, J. A. Di Paola and K. B. Neeves, *Langmuir*, 2011, **27**, 13648–13658.
27 W. H. McAdams and W. H. McAdams, *Heat Transmission*, McGraw-Hill, New York, 1954, vol. 3.
28 W. Bergmeier and R. O. Hynes, *Cold Spring Harbor Perspect. Biol.*, 2012, **4**, 1–17.
29 O. Inoue, K. Suzuki-Inoue and Y. Ozaki, *J. Biol. Chem.*, 2008, **283**, 16279–16282.
30 G. T. Roberts, H. Ghebeh, M. A. Chishti, F. Al-Mohanna, R. El-Sayed, F. Al-Mohanna and A. Bouchama, *Arterioscler., Thromb., Vasc. Biol.*, 2008, **28**, 1130–1136.

31 B. V. Harmon, A. M. Corder, R. J. Collins, G. C. Gobé, J. Allen, D. J. Allan and J. F. R. Kerr, *Int. J. Radiat. Biol.*, 1990, **58**, 845–858.

32 A. N. Bos, M. J. Post, P. G. de Groot, J. J. Sixma and C. Borst, *Circulation*, 1993, **88**, 1196–1204.

33 B. Hechler, C. Nonne, A. Eckly, S. Magnenat, J. Y. Rinckel, C. V. Denis, M. Freund, J. P. Cazenave, F. Lanza and C. Gachet, *J. Thromb. Haemostasis*, 2010, **8**, 173–184.

34 T. Bombeli, A. Karsan, J. F. Tait and J. M. Harlan, *Blood*, 1997, **89**, 2429–2442.

35 T. Bombeli, B. R. Schwartz and J. M. Harlan, *Blood*, 1999, **93**, 3831–3838.

36 L. A. Sporn, V. J. Marder and D. D. Wagner, *Cell*, 1986, **46**, 185–190.

37 P. André, C. V. Denis, J. Ware, S. Saffaripour, R. O. Hynes, Z. M. Ruggeri and D. D. Wagner, *Blood*, 2000, **96**, 3322–3328.

38 J. M. E. M. Cosemans, S. E. M. Schols, L. Stefanini, S. de Witt, M. A. H. Feijge, K. Hamulyak, H. Deckmyn, W. Bergmeier and J. W. M. Heemskerk, *Blood*, 2011, **117**, 651–660.

39 A. K. Chauhan, J. Kisucka, C. B. Lamb, W. Bergmeier and D. D. Wagner, *Blood*, 2007, **109**, 2424–2429.

40 O. Inoue, K. Suzuki-Inoue, O. J. T. McCarty, M. Moroi, Z. M. Ruggeri, T. J. Kunicki, Y. Ozaki and S. P. Watson, *Blood*, 2006, **107**, 1405–1412.

41 S. Gruner, M. Prostredna, V. Schulte, T. Krieg, B. Eckes, C. Brakebusch and B. Nieswandt, *Blood*, 2003, **102**, 4021–4027.

42 O. Inoue, K. Suzuki-Inoue and Y. Ozaki, *J. Biol. Chem.*, 2008, **283**, 16279–16282.

43 K. A. Barbee, T. Mundel, R. Lal and P. F. Davies, *Am. J. Physiol.: Heart Circ. Physiol.*, 1995, **268**, H1765–H1772.

44 J. L. Sylman, S. M. Lantvit, M. C. VeDepo, M. M. Reynolds and K. B. Neeves, *Ann. Biomed. Eng.*, 2013, **41**, 2193–2205.

45 J. L. Sylman, S. M. Lantvit, M. M. Reynolds and K. B. Neeves, *Cell. Mol. Bioeng.*, 2014, **7**, 421–431.

46 S. P. Desai and J. Voldman, *Integr. Biol.*, 2011, **3**, 48–56.

47 D. R. Lide, *CRC Handbook of Chemistry and Physics*, CRC Press, 85th edn, 2004.

48 J.-L. Lai, C.-J. Liao and G.-D. Su, *Sensors*, 2012, **12**, 16390–16403.

49 J. E. Mark, *Polymer Data Handbook*, Oxford University Press, USA, 2009.

50 J. M. Johnson, G. L. Brengelmann, J. R. Hales, P. M. Vanhoutte and C. B. Wenger, *Fed. Proc.*, 1986, **45**, 2841–2850.

51 D. Green and R. Perry, *Perry's Chemical Engineers' Handbook*, McGraw Hill Professional, 8th edn, 2007.

